Article (refereed) – Published version

Seasonal variability of the Red Sea, from satellite gravity, radar altimetry, and in situ observations

John Wahr[1], David A. Smeed[2], Eric Leuliette[3], and Sean Swenson[4]

[1]Department of Physics and Cooperative Institute for Environmental Studies, University of Colorado at Boulder, Boulder, Colorado, USA, [2]National Oceanography Centre, Southampton, UK, [3]Laboratory for Satellite Altimetry, National Oceanic and Atmospheric Administration, College Park, Maryland, USA, [4]National Center for Atmospheric Research, Boulder, Colorado, USA

Abstract Seasonal variations of sea surface height (SSH) and mass within the Red Sea are caused mostly by exchange of heat with the atmosphere and by flow through the strait opening into the Gulf of Aden to the south. That flow involves a net mass transfer into the Red Sea during fall and out during spring, though in summer there is an influx of cool water at intermediate depths. Thus, summer water in the south is warmer near the surface due to higher air temperatures, but cooler at intermediate depths. Summer water in the north experiences warming by air-sea exchange only. The temperature affects water density, which impacts SSH but has no effect on mass. We study this seasonal cycle by combining GRACE mass estimates, altimeter SSH measurements, and steric contributions derived from the World Ocean Atlas temperature climatology. Among our conclusions are: mass contributions are much larger than steric contributions; the mass is largest in winter, consistent with winds pushing water into the Red Sea in fall and out during spring; the steric signal is largest in summer, consistent with surface warming; and the cool, intermediate-depth water flowing into the Red Sea in spring has little impact on the steric signal, because contributions from the lowered temperature are offset by effects of decreased salinity. The results suggest that the combined use of altimeter and GRACE measurements can provide a useful alternative to in situ data for monitoring the steric signal.

1. Introduction

Seasonal variations of mass and sea surface height in the Red Sea are caused mostly by the exchange of heat with the atmosphere and by the inflow and outflow of water through the strait of Bab el Mandab opening into the Gulf of Aden to the south [e.g., *Sofianos and Johns*, 2001; *Smeed*, 2004]. The flow of water through the Bab el Mandab occurs through a complicated, multilayer pattern [see e.g., *Sofianos et al.*, 2002; *Smeed*, 2004]. During the fall, winds blowing from the SSE cause a net northward flow of cool, near-surface water into the Red Sea. The winds reverse direction in spring, causing a net outflow of seasonally warm, near-surface water. Thus, the vertically integrated water mass in the Red Sea is largest in winter and smallest in summer. In addition to this near surface flow, there is significant, summer influx of cool water at intermediate (~100 m) depths, and an outflow at greater depths in the winter. Consequently, summer water in the southern Red Sea is warmer near the surface (due to higher air temperatures) but cooler at intermediate depths. In the northern Red Sea, the summer temperatures are at or above the winter temperatures at all depths. The temperature profile affects the water density, which impacts the sea-surface height (SSH) but has no effect on vertically integrated mass.

This steric contributions to SSH variability can be determined from in situ measurements of temperature and salinity. They can also be indirectly inferred by differencing altimeter SSH and GRACE (Gravity Recovery and Climate Experiment) mass measurements. Similarly, variations in the vertically integrated water mass can be estimated either directly from GRACE, or by subtracting the in situ-derived steric signal from altimeter SSH results.

Suppose $\Delta SSH(\theta, \phi, t)$ and $\Delta\sigma(\theta, \phi, t)$ are variations (relative to some arbitrary mean) in SSH and mass-per area at latitude θ, longitude ϕ, and time t. Let $\Delta SSH_{steric}(\theta, \phi, t)$ be the contribution to $\Delta SSH(\theta, \phi, t)$ caused by changes in water density due to changes in either temperature or salinity. Then

$$\Delta SSH(\theta, \phi, t) = \frac{1}{\rho_0}\Delta\sigma(\theta, \phi, t) + \Delta SSH_{steric}(\theta, \phi, t) \tag{1}$$

where ρ_0 is the mean density of ocean water. Rearranging (1) gives:

$$\frac{1}{\rho_0}\Delta\sigma(\theta, \phi, t) = \Delta SSH(\theta, \phi, t) - \Delta SSH_{steric}(\theta, \phi, t); \tag{2}$$

or, alternatively:

$$\Delta SSH_{steric}(\theta, \phi, t) = \Delta SSH(\theta, \phi, t) - \frac{1}{\rho_0}\Delta\sigma(\theta, \phi, t) \tag{3}$$

An altimeter monitors $\Delta SSH(\theta, \phi, t)$, GRACE recovers $\Delta\sigma(\theta, \phi, t)$, and in situ data can be used to estimate $\Delta SSH_{steric}(\theta, \phi, t)$. Below, we will use (2) and (3) to intercompare and assess altimeter, GRACE, and in situ results.

2. Data Analysis

2.1. GRACE Data

We use Release-5 monthly sets of spherical harmonic (Stokes) coefficients of the gravity field from February 2003 to April 2013, generated from level-one GRACE data [*Tapley et al.*, 2004]. We use coefficients from three processing centers: the Center for Space Research (CSR) at the University of Texas, the GeoForschungsZentrum (GFZ) in Potsdam, and the Jet Propulsion Laboratory (JPL).

These GRACE centers use model output to remove the gravitational effects of atmospheric and oceanic mass variability from the satellite data before constructing monthly gravity field solutions. Each center models the nontidal oceanic effects using bottom pressure output from the same six hourly, global, baroclinic ocean model forced with winds and pressure [*Thomas*, 2002]. The centers provide users with monthly averages of the gravity field contributions from the ocean model. We add those averages back to the GRACE gravity field solutions, so that our GRACE Red Sea estimates reflect the total Red Sea mass signal. The bottom pressure at any location includes the weight of both the ocean and the overlying atmosphere. So by adding back the ocean model's monthly averages we are also adding back the effects of atmospheric pressure over the ocean. This is equivalent to adding back just the ocean, but after removing inverted barometer contributions from the ocean signal.

Each monthly GRACE field consists of a set of Stokes coefficients, C_{lm} and S_{lm}, up to degree and order (l and m) 60. We replace the GRACE C_{20} coefficients with C_{20} coefficients inferred from satellite laser ranging [*Cheng et al.*, 2013], and we include degree-one coefficients computed as described by *Swenson et al.* [2008]. We use model results from *A et al.* [2013] to remove contributions from glacial-isostatic-adjustment (GIA) (the GIA contributions are small in this region, and are nonseasonal; so their impact on the seasonal results discussed in this paper would be minimal even if not removed).

To remove leakage from land water storage adjacent to the Red Sea, we use monthly, gridded, global water storage estimates from the GLDAS/Noah hydrology model [*Rodell et al.*, 2004] to estimate land water storage contributions to the Stokes coefficients, which we subtract from the GRACE coefficients. This hydrology model includes contributions from soil moisture, canopy moisture, and snow, but not from groundwater or surface water. The largest source of nearby surface water variability is Lake Nasser in Egypt. To assess its importance, we remove its contributions from the GRACE results by computing the contributions to the GRACE Stokes coefficients caused by a 1 meter rise in Lake Nasser, and scaling those coefficients by the monthly lake level values determined from radar altimetry [*Birkett et al.*, 2011; http://www.pecad.fas.usda.gov/cropexplorer/global_reservoir/]. We find that the contributions to the GRACE seasonal Red Sea estimates from the GLDAS/Noah predictions are small (see below), and that those from Lake Nasser are negligible. For the results described below we subtract the GLDAS/Noah contributions; but, for simplicity, we omit the Lake Nasser correction.

After making these corrections to the GRACE coefficients, we proceed in two directions. First, we fit seasonal (once and twice-per-year) terms and a linear trend to each Stokes coefficient, and combine the once-per-year coefficients together to obtain the amplitude of the annual cycle in the spatial domain. Figure 1 shows
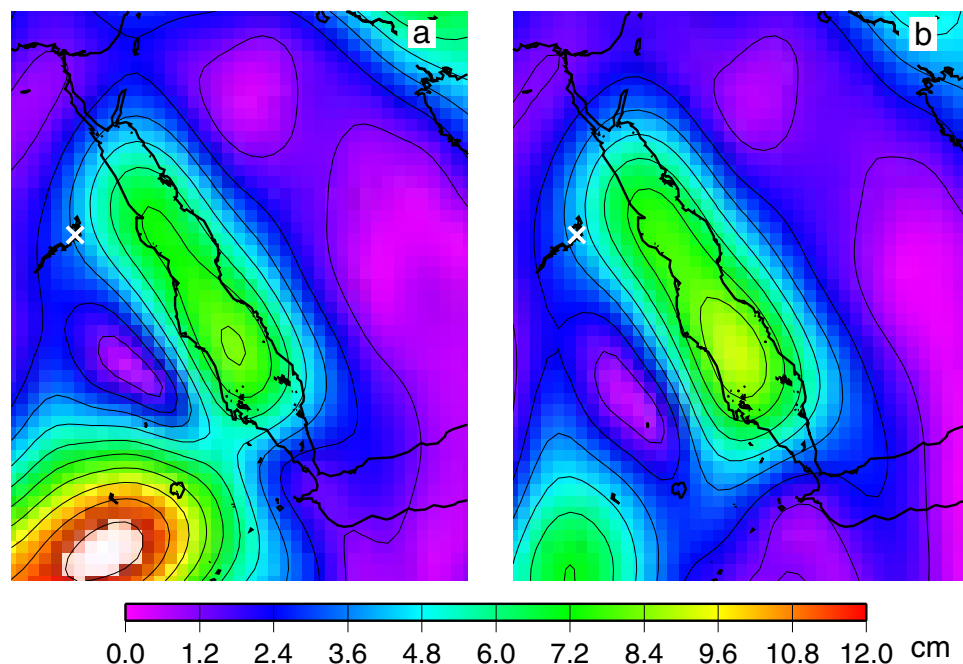
Figure 1. (a) Amplitude of the 1 cycle/yr mass signal, in cm of water thickness, inferred from the February 2003 to April 2013, CSR Release-5 GRACE gravity fields, after the contributions of the de-aliasing ocean model are added back to those fields. The results are smoothed using a Gaussian function with a 300 km radius. Lake Nasser is marked with a white x. Figure 1b is the same as Figure 1a, except after subtracting output from the GLDAS/Noah hydrology model to remove contributions from continental water storage.

the results after applying a Gaussian smoothing function with a half width of 300 km to the CSR Stokes coefficients [*Wahr et al.*, 1998].

Second, we use the Stokes coefficients to construct monthly time series for water mass variations averaged over the northern Red Sea (north of 19° North) and the southern Red Sea (south of 19° North), separately. To do this, we apply an averaging kernel constructed using the weighted convolution approach described in the following section.

2.1.1. A GRACE Averaging Kernel Based on Weighted Gaussian Convolution

We use GRACE to construct monthly solutions, $M(t)$, for mass variations in both the northern and southern Red Sea. Ideally, the solutions for M(t) would recover the true spatial average: i.e., one that samples every point within, say, the northern Red Sea with a sensitivity of 1, and every point outside with a sensitivity of 0. Unfortunately, because of the finite number of harmonic degrees in the GRACE solution (e.g., $l_{max}=60$ for CSR solutions), this is impossible. Any GRACE northern Red Sea solution will sample different points within the northern Red Sea with different weights, and will include some contributions from outside the northern Red Sea. A further complication is that even for $l \leq l_{max}$, the higher-degree coefficients are noisy and so should be suppressed as well.

An effective processing method is one that makes the averaging kernel close to the ideal kernel, though without relying too heavily on the noisy, high-degree Stokes coefficients. We have developed and implemented the following weighted convolution method, that produces an averaging kernel with good sampling and noise characteristics for this region.

Swenson and Wahr [2002, section 4.1] describe an averaging kernel constructed by covering the region with a grid of points, centering a Gaussian averaging function at each point, and summing those averaging functions. A weakness this convolution approach shares with most other analysis methods, is that the final averaging kernel tends to underweight points that are just inside a boundary. This can be a particularly serious problem in a long and narrow region, like the Red Sea, where a large fraction of the region lies near a boundary. This problem can be reduced when there are no sizable external signals to contaminate the solution, by solving for the mass anomaly for a larger region: one that extends out beyond the region of interest [see e.g., *Velicogna and Wahr*, 2006]. In that case, the fact that the result tends to underweight points near

the larger region's boundary causes less of an internal sampling problem, because that boundary is outside the true region of interest. Here we use a slightly different approach; one that is focused on producing near-uniform weighting within the northern (or southern) Red Sea.

We extend Swenson and Wahr's convolution approach by allowing for nonuniform weighting during the convolution. Let $\vartheta(\theta, \phi)$ be the basin function: 1 for points within the region of interest, and 0 for points outside. Swenson and Wahr's convolution averaging kernel is (their equation (29)):

$$\overline{W}(\theta, \phi) = \int_{earth} W(\alpha)\vartheta(\theta', \phi')\sin\theta' d\theta' d\phi' \qquad (4)$$

where $W(\alpha)$ is a Gaussian smoothing function of some chosen radius, and α is the angle between (θ, ϕ) and (θ', ϕ'). If an averaging kernel is expanded in spherical harmonics, the coefficients of those harmonics can be multiplied by the GRACE Stokes coefficients and summed to determine the region's mass variability [*Swenson and Wahr*, 2002, equations (26) and (27)].

The result (4) is equivalent to centering a Gaussian smoothing function at each Red Sea point (θ', ϕ'), and adding together all those Gaussians. The reason that (4) underweights points near a boundary, is that whereas an interior point, (θ, ϕ), is covered by Gaussian averaging functions that extend out from points (θ', ϕ') on all sides of it, a point (θ, ϕ) near the boundary has points (θ', ϕ') on only one side. Thus, a boundary point is covered by fewer Gaussian functions, and so is underweighted.

To reduce this effect, we modify (4) to accommodate nonuniform weighting of the Gaussians:

$$\overline{W}(\theta, \phi) = \int_{earth} W(\alpha)\vartheta(\theta', \phi')F(\theta', \phi')\sin\theta' d\theta' d\phi' \qquad (5)$$

where $F(\theta', \phi')$ is the convolution weighting function. $F(\theta', \phi')$ should be larger near the boundary than in the interior to compensate for the fact that boundary points are covered by fewer Gaussian functions. We use an iterative process to find the function, $F(\theta', \phi')$, that makes $\overline{W}(\theta, \phi)$ as uniform as possible across the region. We start by assuming $F(\theta', \phi')=1$ (i.e., uniform weighting; see (4)), and use (5) to compute $\overline{W}(\theta, \phi)$ at every point (θ, ϕ) within the region. Ideally, the values of $\overline{W}(\theta, \phi)$ would all equal 1.0; but, of course, they would not. We then define $F(\theta', \phi')$ to be $1.0/\overline{W}(\theta, \phi)$, use this new $F(\theta', \phi')$ in (5), and compute new values of $\overline{W}(\theta, \phi)$ at every interior point. Those values should now be closer to 1.0. We repeat the process, defining the new value of $F(\theta', \phi')$ to be 1.0/(previous value of $\overline{W}(\theta', \phi')$), and iterate until reaching convergence. For both the northern and southern Red Sea we use a Gaussian radius of 250 km and 15 iterations; though convergence is reached well before then.

The resulting averaging kernels are shown in Figure 2. Both kernels are reasonably uniform within their respective regions, but extend for a distance outside. This is the price we pay for increasing the weighting of Gaussians centered at near-boundary points. The extension over adjacent land is not likely to be a serious problem, since there is not apt to be significant land water storage variability there. Though this extension does make it more important to correct for any land water storage signals that might exist, by removing the output from a hydrological model.

The extension of the averaging kernels into adjacent oceanic regions causes some of the southern Red Sea signal to leak into the northern Red Sea solution, and vice versa. It also causes some of the signal from the western Gulf of Aden to leak into the southern Red Sea solution. This means that our GRACE results for, say, the southern Red Sea do not exactly correspond to true southern Red Sea averages. On the other hand, much of the focus of our study involves the comparison of GRACE results with altimeter and in situ measurements. For consistency, we will apply the same averaging kernels shown in Figure 2 to these altimeter and in situ measurements. Thus, the results from each data type will mis-sample the southern (and northern) Red Sea in the same way.

We compute the temporal mean of each GRACE Stokes coefficient over the 10+ year time span, and subtract that mean from the monthly values of that coefficient so that the residuals represent the monthly departures from the mean. We convolve each monthly set of residual Stokes coefficients with the averaging kernels described above, to obtain an estimate of the change in water mass per area averaged over the northern and southern Red Seas, separately.
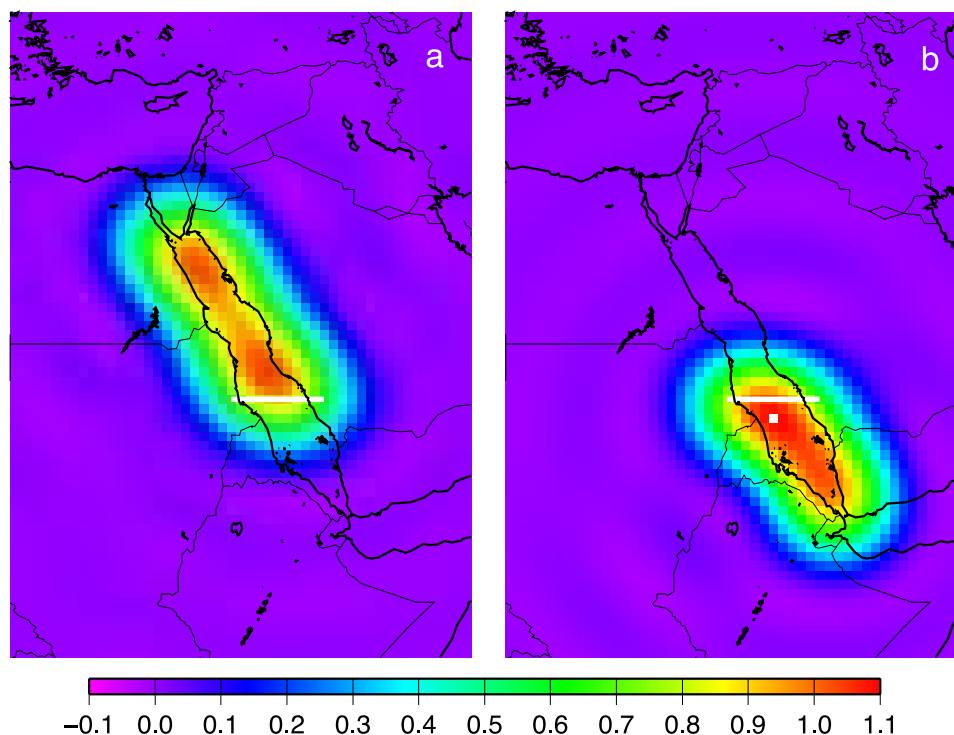
Figure 2. GRACE averaging kernels used to find mass variability of the (a) northern and (b) southern Red Sea. The horizontal white line running across the Red Sea is at 19° North latitude, and marks the dividing line between our definitions of the northern and southern Red Sea.

Our averaging kernel for, say, the northern Red Sea is more uniform across the northern Red Sea than kernels we constructed during the early phases of this project, that were based on other methods (e.g., uniform convolution (4); the optimal averaging kernel described in *Swenson and Wahr* [2002, equation (41)]; and the mascon fitting method described by *Jacob et al.* [2012]) . Still, Figure 2 shows that even our kernel is not exactly unity across the northern Red Sea. In fact, we have imposed no requirement that the average of our kernel over the entire northern Red Sea = 1.0; which means there could be a bias in our averaging kernel that would cause us to systematically under or overestimate the true signal. To determine and correct for this bias we adopt the following procedure. We construct a set of simulated Stokes coefficients which represents the signal from a uniformly distributed, 1 cm water thickness change over the northern Red Sea. We apply our GRACE analysis procedure to these simulated Stokes coefficients, to infer an average water thickness change for the northern Red Sea. Suppose we obtain a thickness change of x. If x $\neq$ 1 cm, then our results are biased. To correct our real GRACE results for this bias, we multiply each monthly GRACE estimate of northern Red Sea mass by a scaling factor = 1 (cm)/x (cm) to obtain variations in the total mass per area of the northern Red Sea. We repeat this procedure for the southern Red Sea. These same scaling factors are applied to the altimeter and in situ estimates, as well.

Once we obtain monthly values for the mass-per-area of each region, we generate a smooth, seasonal time series by simultaneously fitting 12 month and 6 month terms to those values. We apply this same procedure to extract seasonal signals from the altimeter and in situ time series discussed below.

2.2. Altimeter Data

For our analysis of altimeter data, we use the Radar Altimeter Database System [RADS; http://rads.tudelft.nl/], an open source database and analysis package that is continually updated with new data, corrections, and ancillary fields that are consistent among all altimetry missions [*Leuliette and Scharroo*, 2010]. For our 2003–2013 time period we extract all 1 Hz sea surface height (SSH) observations from three altimeter missions (Jason-1, Jason-2, and Envisat) in the region of the Red Sea bounded from 27.5°E to 48° E and 7.5°N to 32.5°N.

While the Jason altimeters observe the Red Sea continuously from a 10 day repeat "reference" ground track, additional spatial coverage varies over the time period. Envisat operated from March 2002 until April 2012.

Its orbit was sun-synchronous with a 35 day repeat until October 2010 when it was maneuvered to a 30 day repeat orbit. From February 2009 to February 2012 Jason-1 operated in an interleaved ground track with a time lag relative to Jason-2 of approximately five days. Jason-1 began a geodetic mission on May 2012, entering a new orbit with a repeat cycle of 406 days that provided a high geographical distribution of observations over time, with a 10.9 day "near-repeat" subcycle. Contact with Jason-1 was lost on 21 June 2013 after 420 days on the geodetic groundtrack.

The Jason-1, Jason-2, and Envisat data in RADS are primarily GDR-D standards. The Jason wet path delays are produced with an algorithm that improves the performance closer to the coast, which is particularly important in a region like the Red Sea where many radiometer retrievals are partially biased by land within the antenna footprint. When applied to 1 Hz path delays from the Jason-2 radiometer, the algorithm error is estimated to be less than 0.8 cm up to 15 km from land, less than 1.0 cm within 10 km from land, less than 1.2 cm within 5 km from land and less than 1.5 cm up to the coastline [*Brown et al.*, 2009].

We reference our SSH values to the DTU10 mean sea surface [*Andersen and Knudsen*, 2009], which uses a reference period of 1993–2009 and provides a gridded spatial resolution of 1 minute of a degree. An inverse barometer correction from ECMWF+MOG2D [*Carrère and Lyard*, 2003] is applied. We use the GRACE Red Sea averaging kernels discussed in section 2.1.1 to construct spatial averages of the 1 Hz SSH observed from all three missions during each month.

2.3. Steric Heights Computed From In Situ Temperature Data

We use the monthly climatological record of gridded, depth-dependent, statistical mean temperatures provided by the World Ocean Atlas, 2009 (WOA09) [*Locarnini et al.*, 2010] to estimate the seasonal steric signal in the Red Sea. The WOA09 record consists of ocean temperature values given on a global $1°$ latitude/longitude grid, at 24 unevenly spaced vertical levels from the surface to 1500 m depth. We use results from just the first 20 vertical levels, extending down to 1100 m, because the WOA09 records in this region show little temperature variability at deeper levels. Twelve monthly temperature values are provided at each lat/lon/depth grid point, one for each month of the year (Jan, etc). Thus, for example, the January value is the average of all in situ, January observations made within that grid element over many decades.

At each lat/lon/depth grid point, we convert the monthly temperature values to monthly density values, using the expression for seawater density as a function of temperature and pressure given by the Thermodynamic Equation of Sea Water, 2010 (TEOS10) [*Feistel*, 2003]. We use subroutines from the Gibbs Sea Water Oceanographic Toolbox [*McDougall and Barker*, 2011] to implement the TEOS10 expressions. We assume a uniform and constant absolute salinity of 35 g/kg .

We use these density values to compute the steric height variations. Let the density at latitude θ, longitude ϕ, height above the sea floor z, and time t, be $\rho(\theta, \phi, z, t)$. Let the height of the sea surface above the sea floor at this same latitude, longitude, and time, be $h(\theta, \phi, t)$. The total mass in the water column is

$$M(\theta, \phi, t) = \int_{z=0}^{h(\theta,\phi,t)} \rho(\theta, \phi, z, t)dz \tag{6}$$

Let $\rho_0(\theta, \phi, z)$ and $h_0(\theta, \phi)$ be the density and sea surface height the column would have if the water was at $0°$C everywhere. Define the density and steric height anomalies as

$$\Delta\rho(\theta, \phi, z, t) = \rho(\theta, \phi, z, t) - \rho_0(\theta, \phi, z) \tag{7}$$

and

$$\Delta h(\theta, \phi, t) = h(\theta, \phi, t) - h_0(\theta, \phi) \tag{8}$$

Using (7) and (8) in (6), and assuming the density and steric height anomalies are small, then to first order in small quantities (6) reduces to:

$$M(\theta, \phi, t) = \int_{z=0}^{h_0(\theta,\phi)} \rho_0(\theta, \phi, z)dz + \int_{z=0}^{h_0(\theta,\phi)} \Delta\rho(\theta, \phi, z, t)dz + \Delta h(\theta, \phi, t)\rho_0(\theta, \phi, z=0) \tag{9}$$

For a steric signal, the mass $M(\theta, \phi, t)$ does not change with time. The first integral on the right-hand side of (9) is also time independent. So (9) implies that to within a time-independent constant:

$$\Delta h(\theta, \phi, t) = \frac{-1}{\rho_0(\theta, \phi, z=0)} \int_{z=0}^{h_0(\theta,\phi)} \Delta\rho(\theta, \phi, z, t)\,dz \tag{10}$$

We use the TEOS10 expressions to obtain results for $\rho(\theta, \phi, z, t)$, $\rho_0(\theta, \phi, z)$, and $\rho_0(\theta, \phi, z=0)$, and so to infer $\Delta\rho(\theta, \phi, z, t)$, at every WOA09 lat/lon/depth grid point, for each of the 12 months. We integrate over depth, as described by (10), to obtain a time-dependent steric height estimate at every 1° lat/lon grid point.

A 1° lat/lon grid spacing is coarse relative to the east-west scale of the Red Sea, and so taking the union of all WOA09 ocean grid elements results in blocky, irregular coverage. This problem is further complicated because WAO09 does not report values for some of the oceanic lat/lon grid points in the southern Red Sea and western Gulf of Aden. To improve the coverage we construct a finer oceanic grid, with 1/12° lat/lon spacing, that covers the entire Red Sea and Gulf of Aden. We interpolate the steric height results computed on the WOA09 grid, to this finer grid. We average the resulting lat/lon values together to get average steric height values for the northern and southern Red Sea for each month, which, we construct by weighting the data using the GRACE averaging kernels described in section 2.1.1. We include steric height values in the Gulf of Aden, since the averaging kernels are nonzero there, particularly for the southern Red Sea. We use these nonuniformly weighted results to compare with the GRACE and altimeter results, since then the results from all three data types sample the ocean in the same way.

The orange lines in Figure 3 show the monthly values of the steric signals computed from the WOA09 temperature data, and weighted using the GRACE averaging kernel. The signal in the northern Red Sea is dominated by a 12 month periodic term, with a maximum in late summer. This term is caused by the expansion of upper ocean layers due to summer atmospheric warming. The time series in the southern Red Sea is more complicated, and shows a sharp decrease and subsequent recovery during late summer. By looking at the steric signal at individual grid points (not shown), we find that this summertime dip occurs at Red Sea points with latitudes below 15° N, but not at higher latitudes. At those lower latitudes the summertime temperature variations causing this dip are prominent only at depths below 75 m. At shallower depths, the temperatures at these low-latitude grid points are maximum in summer, just as in the rest of the Red Sea. This summertime cooling at depth is caused by the influx of intermediate-depth cold water from the Gulf of Aden.

2.4. Salinity Effects

The orange lines in Figure 3 include the effects of temperature, but not of salinity. When we use WOA09 salinity values in the TEOS10 density expressions, we obtain large, spurious, time-varying signals in the steric sea level heights. We suspect this is due to errors in the gridded salinity values caused by the sparse number of Red Sea salinity observations. At every Red Sea grid point, at least 5 times as many temperature as salinity observations are used to determine the monthly WOA09 values. Usually that disparity is much greater. At every grid point in the northern Red Sea, for example, the ratio is larger than 14. In fact, there are several grid points in the Red Sea that have no, or perhaps just one, salinity observation for at least some of the months. Furthermore, there is often considerable systematic, temporal variability in the number of salinity observations at a grid point: e.g., a couple months with virtually no observations, followed by a month or two with a greatly increased number of observations, etc. This irregular sampling could introduce large errors that have a systematic time dependence.

Instead, we estimate the salinity effects by modifying the WOA09 temperature values at each lat/lon/depth grid point in the Red Sea (but not in the Gulf of Aden), so that the value of the temperature in any month never falls below the March value at that grid point. If a grid point's temperature value is smaller than in March, we reset it to the March value; otherwise, we leave it unchanged.

Our rationale is that most of the seasonal salinity variations come from the summertime intrusion of cold, fresh water into the Red Sea from the Gulf of Aden. This intrusion occurs at an intermediate level below the mixed layer but above the sea floor. The cooler temperature makes the water denser, but its freshness makes it less dense. So the use of temperature alone predicts a steric height in summer that is too low. Because the intrusion is at an intermediate level it seems reasonable to assume that the intruding water displaces water of a similar density, so that the net effect on the steric height is negligible. March is the month with the lowest temperature for most Red Sea grid points. But the intrusion of this cool water causes the
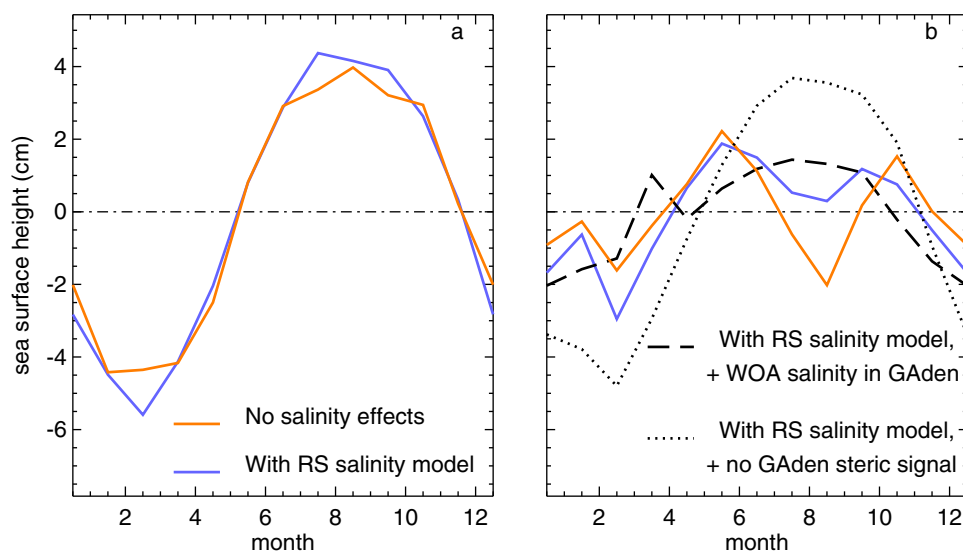
Figure 3. Time series showing the steric contributions to sea surface height in the (a) northern and (b) southern Red Sea, computed using the WOA09 temperature and salinity fields. The orange lines show contributions from temperature anomalies alone. For the blue lines in Figures 3a and 3b, and the dashed and dotted lines in Figure 3b, Red Sea salinity contributions are included by modifying the WOA09 temperature fields so that the monthly temperature at each grid point is never allowed to fall below its March value. For the blue lines, no salinity corrections are made for points in the Gulf of Aden. In Figure 3b, the dashed black line includes salinity contributions from the Gulf of Aden, computed using the WOA09 salinity values. The dotted black line omits all contributions (from both temperature and salinity) from the Gulf of Aden.

summertime temperature of the intermediate-depth water in the southern-most portion of the Red Sea, to fall below its March value. By resetting the temperature so that it never drops below its March value, we are removing the impact of the intruding water on the steric signal. Basically, we are taking the view that if we cannot accurately include the effects of salinity, it is better to ignore the effects of temperature in the intermediate intrusion.

The blue lines in Figure 3 show the results when this salinity correction is applied to the temperature fields. The effect on the northern Red Sea results is clearly small: it increases the seasonal cycle amplitude by only 8%, and has little impact on the phase. The effect on the southern Red Sea results is more important. There, the peak-to-peak amplitude of the seasonal steric signal is not notably different: salinity increases that amplitude by less than 20%. But, after including the salinity correction, the steric signal is more clearly dominated by a 12 month term with a summertime maximum. There is still a dip in mid-summer, but it is less prominent. For all the WOA09 results described below, we include this salinity correction.

The remaining summertime dip is due to the signal in the western Gulf of Aden leaking into the southern Red Sea results because of the imperfect averaging kernel. The dotted black line in Figure 3b shows the steric signal after the Red Sea salinity correction is applied, and after removing all Gulf of Aden points when computing the southern Red Sea average. The summertime dip is now gone, leaving only a 12 month component with a maximum in the summer.

But, it would be incorrect to use a steric signal that omits the Gulf of Aden when comparing with the GRACE results, since GRACE does sample the Gulf of Aden. To assess the effects of Gulf of Aden salinity, we use the WOA09 Gulf of Aden salinity values, along with the WOA09 temperature values throughout the Gulf of Aden and the Red Sea (applying the Red Sea salinity correction described above), in the TEOS10 density expressions, and weight with the southern Red Sea GRACE averaging kernel to estimate the steric signal in the southern Red Sea. We obtain the results shown by the dashed black line in Figure 3b. Although these results are less jagged than the results where no Gulf of Aden salinity effects have been included (the blue line), the two sets of results look similar after smoothing (not shown).

In the remainder of this paper we use steric estimates which include the effects of temperature but not salinity in the Gulf of Aden. The reason is that although the salinity sampling problem is somewhat better at grid points in the western portion of the Gulf of Aden (i.e., near the Red Sea) than it is in the Red Sea, the
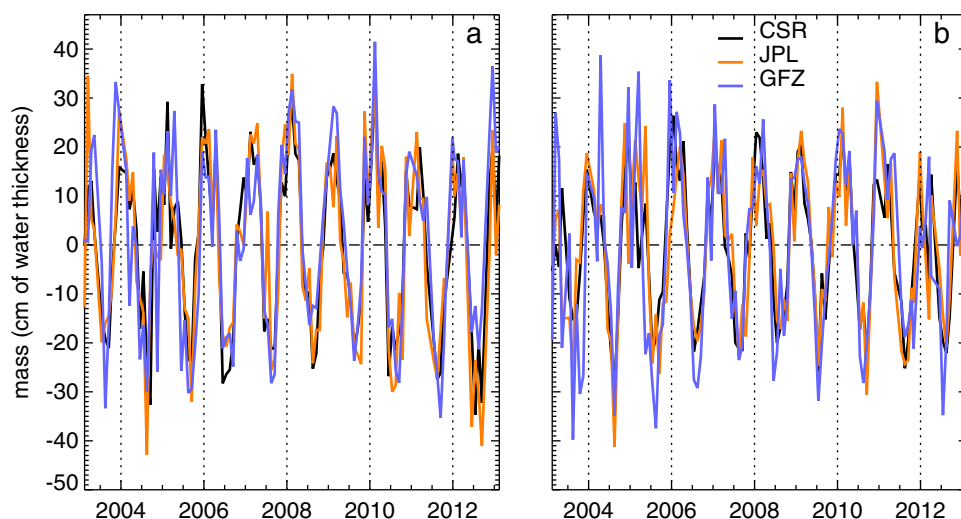
Figure 4. Time series showing changes in the spatially averaged mass-per-area of the (a) northern and (b) southern Red Sea, from the CSR, JPL, and GFZ GRACE gravity field solutions.

problem is still challenging. Some of those Gulf of Aden grid points have several times the number of salinity observations than those in the southern Red Sea. But, there are still roughly ten times as many temperature observations as salinity observations at those Gulf of Aden grid points.

3. Results

The amplitude of the annual cycle of the GRACE mass/area results (Figure 1), shows an obvious signal confined to the Red Sea. Figures 1a and 1b show the amplitude before and after using output from the GLDAS/Noah hydrology model to remove the continental water storage signal. Figure 1a shows that even before removing GLDAS/Noah, the Red Sea signal is isolated from any comparable seasonal cycle on land. This isolation is even more striking once the GLDAS/Noah output has been removed (Figure 1b). The isolation of the Red Sea signal implies that the fact that our GRACE Red Sea averaging kernels extend out over land (Figure 2) is not apt to cause significant contamination of our results.

Note that there is no obvious annual signal from Lake Nasser (white x in Figure 1). The results shown in Figure 1 and in the time series plots below, have not had the Lake Nasser signal removed. We find, though, that when we do remove that signal (see above), there is no discernible impact either on these maps or on the time series results.

Figure 4 shows the monthly GRACE mass estimates for the two regions, computed using Stokes coefficients from each of the three GRACE processing centers. The RMS of the differences between the results for the three centers are roughly 10 cm, and are about the same for the two regions. The differences between the three sets of results reflect differences in how the centers process the raw GRACE data to recover Stokes coefficients. Each month is processed separately from every other month, and the three centers remove the same atmospheric and ocean tide models from the raw data before processing. These facts suggest that differences between the three sets of GRACE fields should look more-or-less random from one month to the next, so that differences between seasonal terms that are fit to the monthly data should be due mostly to month-to-month random errors rather than to systematic seasonal differences (though, see section 3.1).

Table 1 shows the RMS of the GRACE time series for the three centers, after the best-fitting seasonal (i.e., 12 and 6 month terms) signal has been removed. The CSR fields have the smallest RMS, which suggests those fields might provide the most accurate seasonal solutions. But the RMS values are close enough that we have opted, instead, to simply average together all three solutions and to use that average as our preferred GRACE solution. Table 1 shows that the average of the three solutions has an RMS about its seasonal cycle that's roughly equal to that of the CSR fields alone. We will continue, though, to show results from each center individually when discussing the seasonal components.

Table 1. RMS Values of the GRACE Mass/Area Solutions (in cm of Equivalent Water Thickness), About the Best-Fitting Seasonal Signal, for the February 2003 to April 2013 Release-5 GRACE Gravity Solutions[a]

GRACE Center	Northern Red Sea (cm)	Southern Red Sea (cm)
CSR	7.7	6.5
GFZ	11.0	11.8
JPL	10.3	9.3
Average of three centers	7.4	6.5

[a]Results are shown for fields from each of the three GRACE processing centers, and for the average of those fields.

Figure 5 compares the average of the three GRACE mass/area time series, with the altimeter sea surface height results and the WOA09 estimates of the steric signal. The steric values shown in the figure are not the actual values for each specific month during this ~10 year time span. Instead, they are the WOA09 climatology values, repeated every year.

Figure 5 shows that (a) the time variability is dominated by seasonal fluctuations; (b) the mass contributions to SSH are much larger than the steric contributions; (c) the seasonal mass and steric contributions are roughly 6 months out-of-phase with one another, with the mass variations peaking in the winter and the steric signal peaking in the summer. Point (c) is consistent with the hypothesis that the steric signal is dominated by the exchange of heat with the atmosphere (in summer, when the atmospheric temperatures are high, the near-surface ocean temperatures are also high and the water expands), whereas the mass signal is dominated by the fall inflow (spring outflow) of water from (to) the Gulf of Aden.

Note that the steric signal has a more complicated time dependence in the southern Red Sea than in the northern Red Sea. The northern signal appears as almost a pure 12 month term, whereas the signal in the south contains additional components. This difference, which was discussed above, occurs because of leakage of the Gulf of Aden signal into the southern Red Sea solution, caused by the imperfect GRACE averaging kernel.

3.1. The Seasonal Cycle

We fit seasonal (12 and 6 month) terms to the GRACE mass values, the altimeter SSH results, and the WOA09 steric values, and plot the resulting seasonal variability in Figures 6 and 7. For GRACE, we show results for the average of the three solutions (solid black line) and for the individual solutions (dotted black lines). The three GRACE solutions cluster closely about one another, particularly for the northern Red Sea.

The conclusions from these seasonal results are the same as those inferred from Figure 5: the mass variability is much larger than the steric signal, and is 6 months out-of-phase with it. We can help establish a level of confidence in these conclusions by comparing linear combinations of mass, SSH, and steric results.
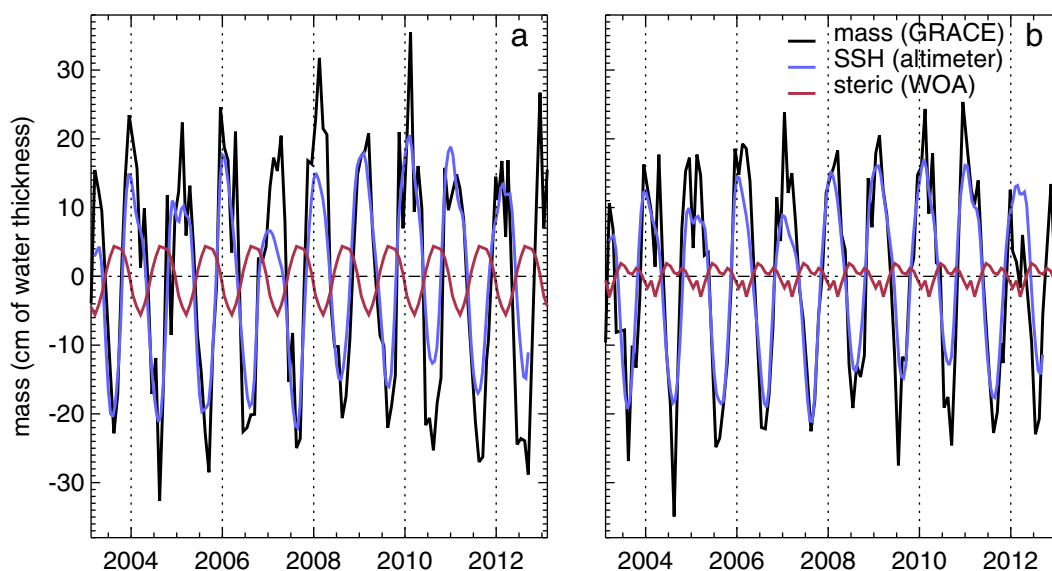

Figure 5. Time series of the GRACE mass-per-area results (the average of the CSR, JPL, and GFZ results), the altimeter sea surface height (SSH) results, and the steric results estimated from the World Ocean Atlas (WOA09) values, for the (a) northern and (b) southern Red Sea. The steric results are the WOA09 climatology values repeated every year.
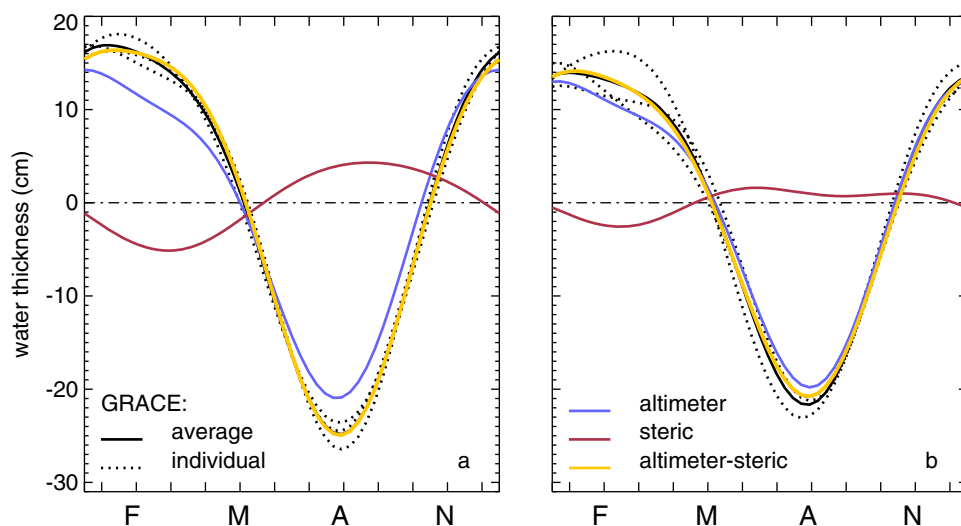
Figure 6. The seasonal components of mass-per-area from GRACE (black), sea surface height from altimetry (blue), the steric signal from the WOA09 values (red), and an estimate of the mass-per-area obtained by subtracting the WOA09 steric signal from the altimeter sea surface height estimate (orange), for the (a) northern and (b) southern Red Sea. The solid black line shows results for the average of the CSR, JPL, and GFZ GRACE results; the dotted black lines show the CSR, GFZ, and JPL GRACE results separately. The tick marks on the x axis are at the midpoints of the months.

For example, (2) implies that the mass contribution to the SSH can be determined by subtracting the WOA09 steric signal from the altimeter SSH values.

The orange lines in Figure 6 show the seasonal altimeter-minus-steric results. There is excellent agreement between those results and the average of the three GRACE solutions. In fact, in many places it is difficult to tell that there's a solid black line underlying the orange line. The RMS of the difference between the altimeter-minus-steric signal and the average of the three GRACE solutions is only 3% of the RMS of the GRACE signal for the northern Red Sea, and 4% for the southern Red Sea. The agreement between the altimeter-minus-steric signal and the results from the individual GRACE solutions, is not as good as the agreement with the average of the GRACE solutions. This suggests that the average is more accurate than
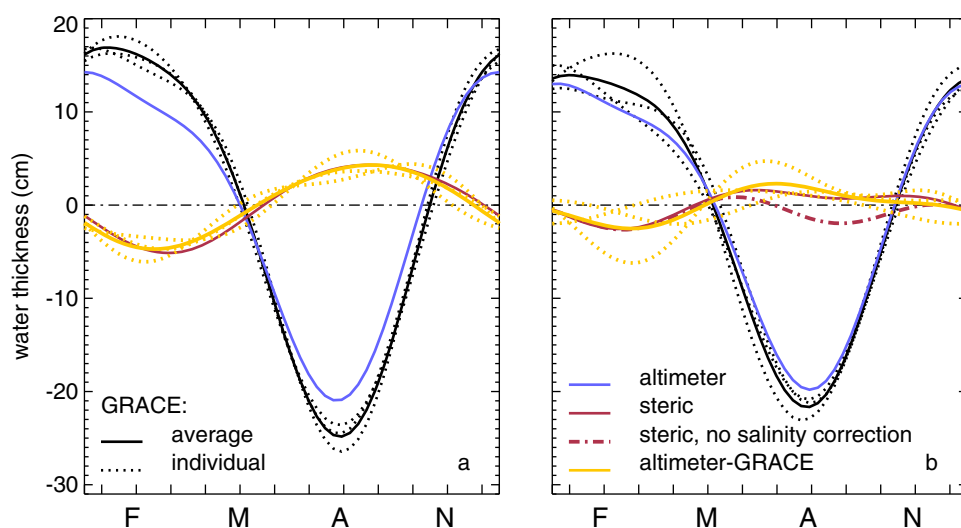

Figure 7. The seasonal components of mass-per-area from GRACE (black), sea surface height from altimetry (blue), the steric signal from the WOA09 values (solid red line), and an estimate of the steric signal obtained by subtracting the GRACE mass-per-area signal from the altimeter sea surface height estimate (orange), for the (a) northern and (b) southern Red Sea. The solid black and orange lines show results for averages of the CSR, JPL, and GFZ GRACE fields. The dotted black and orange lines show results for the CSR, GFZ, and JPL GRACE fields separately. The dashed red line shows the WOA09 steric results computed without including the salinity correction described in the text.

the individual solutions, and implies that the solutions from the different centers contain different systematic errors that tend to offset one another when averaged together.

Another way of comparing the data is suggested by (3), which shows that the steric signal can be estimated by subtracting the GRACE mass values from the altimeter SSH results . The solid orange lines in Figure 7 show the seasonal results obtained by subtracting the average of the three GRACE solutions. Each dotted orange line shows results obtained by subtracting an individual GRACE solution. There is good agreement between the steric estimates from the WOA09 data and those from the altimeter minus the average GRACE data, particularly for the northern Red Sea. The RMS of the difference between the altimeter-minus-GRACE signal (the solid orange line) and the WOA09 steric signal (the solid red line) is 15% of the RMS of the steric signal for the northern Red Sea, and 36% for the southern Red Sea. These percentages are larger than those for the mass comparisons shown in Figure 6, because the steric signals shown in Figure 7 are much smaller than the GRACE signals shown in Figure 6. The steric signal inferred from altimeter-minus-GRACE is the difference between two large and nearly equal sets of numbers, and so is sensitive to relatively small errors in either the altimeter or GRACE results.

The scatter of the dotted orange lines in Figure 7b (the southern Red Sea) might appear to be larger than the scatter of the dotted black lines. But, the numerical values of the scatter are the same; it's just that the steric signal is much smaller than the mass signal, and so the scatter is a larger fraction of the steric signal than of the mass signal.

The dashed red line in Figure 7b shows the WOA09 steric signal computed without including the salinity correction described above. Clearly the inclusion of this correction has a significant impact on the steric estimates, and improves the agreement with the altimeter-minus-GRACE results.

4. Summary and Discussion

Sea surface height variability within the Red Sea has two dominant causes: thermal exchange with the atmosphere, and the exchange of water with the Gulf of Aden through the strait of Bab el Mandab. The effects of atmospheric heat exchange are straightforward. In summer, the upper layers of the ocean become warm and expand, causing the sea surface to rise. This process reverses in winter. The impact of the exchange of water with the Gulf of Aden is more complex. Northward winds over the southern Red Sea force a net influx of water into the Red Sea in the fall, causing an increase in Red Sea mass which raises sea levels in winter. The sea level change is a little greater in the northern Red Sea, but is almost uniform throughout The winds reverse direction in the spring, blowing water southward out of the Red Sea and causing a summer sea level decline. This inflow/outflow of water is not uniform with depth. Throughout most of the year there is a two-layer exchange in which surface waters flow into the Red Sea and deeper waters flow out [e.g., *Sofianos et al.*, 2002, *Smeed*, 2004]. In the summer, the surface flow reverses and there is an influx of water at ∼80 meter depth [*Sofianos et al.*, 2002, *Smeed*, 2004]. This inflowing intermediate water is cool, and leads to a decrease in summer temperatures at those depths, extending at least 300 km north of the Strait of Bab el Mandab. By itself, this temperature decrease would cause an increase in density and so a decrease in SSH at those southern points. But that inflowing water is also relatively fresh, and that tends to decrease the density and so offsets the effects of the cooler temperature. In fact, because the inflowing water occurs within a layer of intermediate depth, at neither the top nor bottom of the water column, it presumably displaces water of equal density. This suggests that the temperature and salinity of the inflowing water conspire so that the water has no net effect on density, and so no net impact on the steric signal.

We use three data types to help quantify these ideas. GRACE data are used to monitor monthly changes in mass within the Red Sea from February, 2003 to April 2013. Altimeter measurements are used to determine monthly variations in SSH during this same time period. And, WOA09 temperature fields, based on in situ measurements, are used to determine the climatologically averaged monthly steric signal: i.e., January, etc. values that are the averages of all January, etc. observations over several decades.

We find that the month-to-month variations in SSH and mass variability are dominated by the sum of 12 and 6 month periodic components, which we refer to as the seasonal signal. The seasonal mass and steric contributions differ in phase by about half a year. The mass variations are maximum in winter and minimum
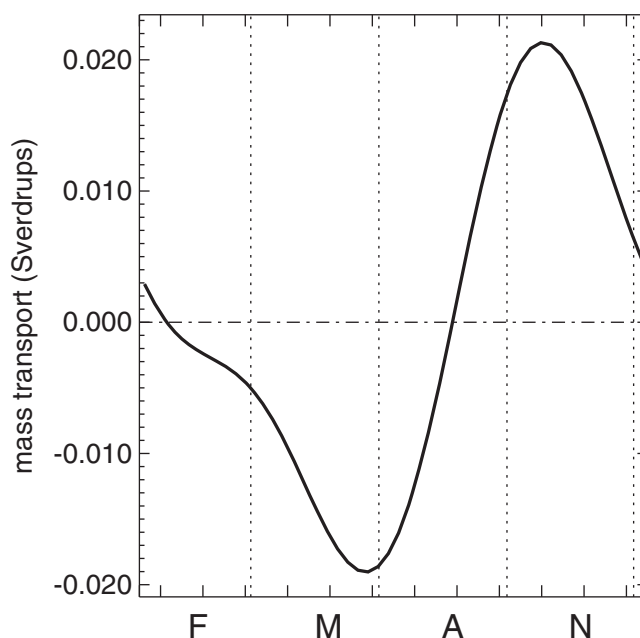
Figure 8. The seasonal component of the transport through the strait of Bab el Mandab, inferred from the GRACE mass estimates. Positive values indicate transport into the Red Sea. The total transport through the strait equals this seasonal component superimposed on a mean flow of about 0.02 Sverdrups [e.g., *Smeed*, 2004], that cannot be determined from the GRACE results. The vertical dotted lines denote the times of the solstices and equinoxes.

in summer, which is consistent with the net fall influx of water from the Gulf of Aden, and subsequent spring outflow [*Sofianos and Johns*, 2001]. The steric contributions are maximum in summer and minimum in winter, which is consistent with surface heating in the summer and cooling in the winter. The peak-to-peak variations in mass appear to be much larger than those from the steric contributions: 4.5 times larger in the northern Red Sea and 8.5 times larger in the southern Red Sea. These different ratios are due to differences in the steric amplitudes in the two regions. The amplitudes of the mass variations are about the same, but the amplitudes of the steric signals are about half as large in the southern Red Sea as in the northern Red Sea. This dif-

ference, though, is misleading. Our southern Red Sea averaging kernel extends a short distance into the western Gulf of Aden. The steric signal there is strong enough to have an appreciable impact on our steric solution. Because of the intense upwelling of colder water during the summer monsoon, the Gulf of Aden signal is out-of-phase with the steric solution in the southern Red Sea, and so causes a notable reduction in the amplitude of the southern Red Sea signal. If the Gulf of Aden contributions are omitted from the steric signal, the peak-to-peak amplitude of the steric signal is about the same in the southern Red Sea as in the northern Red Sea (compare the dotted black line in Figure 3b with the blue line in Figure 3a): the amplitude of the northern solution is only about 15% larger than the amplitude in the south.

The GRACE results allow us to estimate the seasonal variation in mass transport through the Strait of Bab el Mandab. We convert the GRACE seasonal water thickness results shown in Figure 7 into a time series of total Red Sea mass, by multiplying by the areas of the northern and southern Red Seas, and summing We find that the total mass is maximum near the end of January and minimum in mid-August, and that the change in mass between those two dates is ∼170 gtons. We compute the time derivative of that time series to get the seasonal component of the rate of change of total mass. Since variations in total mass are caused by water exchange with the Gulf of Aden, we interpret the rate of change as the seasonal component of mass transport through the strait of Bab el Mandab.

Figure 8 shows this inferred seasonal transport, where positive values denote flow into the Red Sea. This transport varies seasonally by 0.04 Sverdrups, with inflow during spring and early summer, and outflow during fall and late summer. This seasonal transport must be superimposed on a mean transport of 0.02 Sverdrups into the Red Sea [e.g., *Smeed*, 2004], that balances the near-constant loss of mass through evaporation from the Red Sea surface, but that cannot be determined from the GRACE data.

We compare linear combinations of the SSH, mass, and steric signals to help assess the validity of our conclusions. We compare two estimates of seasonal mass variability: one from GRACE and one obtained by subtracting the WOA09 steric signal from the altimetry SSH signal. We also compare two estimates of the seasonal steric signal: one from the WOA09 data and one by subtracting the GRACE mass signal from the altimeter SSH results. There is good agreement in both these cases, as can be inferred from Figures 6 and 7. The agreement is especially encouraging given that the GRACE and altimeter data cover

the same time span, whereas the WOA09 data represent the mean climatological values averaged over decades.

We find there are insufficient salinity data to allow us to accurately calculate the effects of salinity on the steric height using the WOA09 fields. Instead, when using those fields we include the salinity effects indirectly, by modifying the temperature profile to reduce the impact of the summer inflow of cool, intermediate-depth water. We find that this ad hoc correction has a significant impact on our WOA09 steric estimates, resulting in notably better agreement with our altimeter-minus-GRACE results. While the limited amount of in situ hydrographic data are unlikely to be sufficient to monitor long-term steric height changes, our results suggest that the combination of GRACE and altimetry data might be a useful alternative for monitoring long-term changes in the Red Sea.

References

A, G., J. Wahr, and S. Zhong (2013), Computations of the viscoelastic response of a 3-D compressible earth to surface loading: An application to glacial isostatic adjustment in Antarctica and Canada, *Geophys. J. Int.*, *192*, 557–572, doi:10.1093/gji/ggs030.

Andersen, O. B., and P. Knudsen (2009), DNSC08 mean sea surface and mean dynamic topography models, *J. Geophys. Res.*, *114*, C11001, doi:10.1029/2008JC005179.

Birkett, C. M., C. Reynolds, B. Beckley, and B. Doorn (2011), From research to operations: The USDA global reservoir and lake monitor, in *Coastal Altimetry*, edited by S. Vignudelli et al., chap. 2, pp. 19–50. Springer, Berlin.

Brown, S., S. Desai, S. Keihm, and W. Lu (2009), Microwave radiometer calibration on decadal time scales using on-Earth brightness temperature references: Application to the TOPEX microwave radiometer, *J. Atmos. Oceanic Technol.*, *26*, 2579. doi:10.1175/2009JTECHA1305.1.

Carrère, L., and F. Lyard (2003), Modeling the barotropic response of the global ocean to atmospheric wind and pressure forcing, *Geophys. Res. Lett.*, *30*(6), 1275, doi:10.1029/2002GL016473.

Cheng, M. K., B. D. Tapley, and J. C. Ries (2013), Deceleration in the Earth's oblateness, *J. Geophys. Res. Solid Earth*, *118*, 740–747, doi: 10.1002/jgrb.50058.

Feistel, R. (2003), A new extended Gibbs thermodynamic potential of seawater, *Prog. Oceanogr.*, *58*, 43–114, doi:10.1016/S0079-661(03)00088-0.

Jacob, T., J. Wahr, T. Pfeffer, and S. Swenson (2012), Recent contributions of glaciers and ice caps to sea level rise, *Nature*, *482*(7386), 514–518, doi:10.1038/nature10847.

Leuliette, E. W., and R. Scharroo (2010), Integrating Jason-2 into a multiple-altimeter climate data record, *Mar. Geod.*, *33*, 504–517, doi: 10.1080/01490419.2010.487795.

Locarnini, R. A., A. V. Mishonov, J. I. Antonov, T. P. Boyer, H. E. Garcia, O. K. Baranova, M. M. Zweng, and D. R. Johnson (2010), Volume 1: Temperature, in *World Ocean Atlas 2009, NOAA Atlas NESDIS 68*, edited by S. Levitus, 184 pp., U.S. Gov. Print. Off., Washington, D. C.

McDougall, T. J., and P. M. Barker (2011), Getting started with TEOS-10 and the Gibbs Seawater (GSW) Oceanographic Toolbox, *SCOR/IAPSO WG127*, 28 pp. [Available at http://www.teos-10.org/.]

Rodell, M., et al. (2004), The global land data assimilation system, *Bull. Am. Meteorol. Soc.*, *85*, 381–394.

Smeed, D. A. (2004), Exchange through the Bab el Mandab, *Deep Sea Res., Part I*, *51*, 455–474.

Sofianos, S., and W. Johns (2001), Wind induced sea level variability in the Red Sea, *Geophys. Res. Lett. 28*, 3175–3178.

Sofianos, S. S., W. E. Johns, and S. P. Murray (2002), Heat and freshwater budgets in the Red Sea from direct observations at Bab el Mandeb, *Deep Sea Res., Part II*, *49*, 1323–1340, doi:10.1016/S0967-0645(01)00164-3.

Swenson S., and J. Wahr (2002), Methods for inferring regional surface-mass anomalies from GRACE measurements of time-variable gravity, *J. Geophys. Res.*, *107*(B9), 2193, doi:10.1029/2001JB000576.

Swenson, S., D. Chambers, and J. Wahr (2008), Estimating Geocenter Variations from a Combination of GRACE and Ocean Model Output, *J. Geophys. Res.*, *113*, B08410, doi:10.1029/2007JB005338.

Tapley B. D., Bettadpur S., J. C. Ries, P. F. Thomson, and M. M. Watkins (2004), GRACE measurements of mass variability in the earth system, *Science*, *305* (5683), 503–505.

Thomas, M. (2002), Ocean induced variations of Earth's rotation–Results from a simultaneous model of global circulation and tides, PhD thesis, 129 pp., Univ. of Hamburg, Hamburg, Germany.

Velicogna, I., and J. Wahr (2006), Measurements of time variable gravity shows mass loss in Antarctica, *Science*, *311*, 1754–1756.

Wahr, J., S. Swenson, V. Zlotnicki, and I. Velicogna (2004), Time-Variable gravity from GRACE: First results, *Geophys. Res. Lett.*, *31*, L11501, doi:10.1029/2004GL019779.

Wahr, J., M. Molenaar, and F. Bryan (1998), Time-variability of the Earth's gravity field: hydrological and oceanic effects and their possible detection using GRACE, *J. Geophys. Res.*, *103*, 30205–30230.